J. Fluid Mech. (2009), *vol.* 631, *pp.* 397–417.
doi:10.1017/S0022112009007022 Printed in the United Kingdom

Mid-gap invasion in two-layer slot coating

JAEWOOK NAM[1] AND MARCIO S. CARVALHO[2]†

[1]Coating Process Fundamentals Program, Department of Chemical Engineering and Materials Science, University of Minnesota, MN 55455, USA

[2]Department of Mechanical Engineering, Pontifícia Universidade Católica do Rio de Janeiro, Rua Marques de Sâo Vicente 225, Gávea, RJ 22453-900, Brazil

(Received 28 October 2008 and in revised form 10 March 2009)

Multi-layer, continuous liquid coating is the most efficient way to manufacture films that require more than one layer for optimal performance. Dual-layer slot coating is one of different coating methods largely used to deposit two thin, uniform liquid layers on to a moving substrate. The two liquid phases are separated by an inter-layer that starts at the separation point (or line, in three dimensions) attached to the die surface. The stability of the two-phase flow and the location of the separation point are directly related to the quality of the final product. Ideally, the separation point should be attached to the downstream corner of the mid die piece of a dual slot-coating die. However, its location may change as operating conditions vary, leading to undesired flow states, with microvortices and periodic oscillation. The movement of the separation point from its desired location along the die surface is usually referred to as mid-gap invasion and can be associated with the onset of coating defects. It is crucial to determine the set of flow conditions at which it occurs. We study the evolution of the separation-point location and the inter-layer configuration as a function of operating conditions by flow visualization and by solving the two-dimensional Navier–Stokes equation for free-surface flows. The results reveal two different mechanisms for mid-gap invasion, depending on the viscosity ratio of the two liquid layers. They also show that the most critical parameter responsible for the onset of mid-gap invasion is the bottom-layer wet thickness (flow rate). Although the movement of the separation point involves an evolution of complex flow states, a simple but accurate criterion based on rectilinear flow approximation is proposed.

1. Introduction

Continuous liquid coating is the main manufacturing step in the production of many different products such as adhesive tapes, specialty papers and optical films. It is also a very strong candidate for mass production of nanoparticle assembly films, as discussed by Maenosono, Okubo & Yamaguchi (2003). Slot coating is one of the many existing methods to obtain a thin, uniform liquid layer over a moving substrate. The coating liquid is pumped to a coating die in which the liquid is distributed across the width of a narrow slot. Exiting the slot, the liquid forms a bridge between the moving web and die lips that is bounded by an upstream and downstream gas–liquid interfaces. Slot coating belongs to a class of coating methods known as pre-metred coating: the thickness of the deposited liquid layer is set by the flow rate fed to the coating die and the web speed and is independent of other process variables.

† Email address for correspondence: msc@puc-rio.br

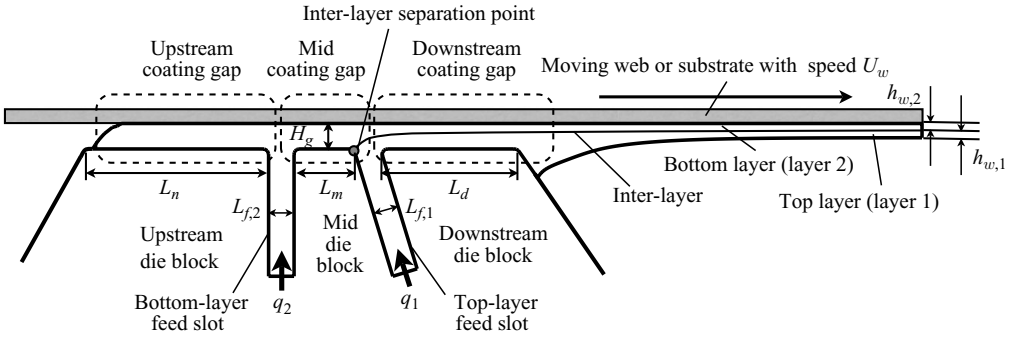

FIGURE 1. Two-layer dual slot-coating schematic diagram. The flow between a moving web and a die lip can be divided into three regions: upstream gap, mid gap and downstream gap regions. Inter-layer starts from mid gap region and passes through downstream coating gap. The layer closes to the substrate is called the bottom layer (phase 2 in the diagram); H_g is the gap height between web and die lip; $h_{w,1}$ and $h_{w,2}$ are the wet thicknesses of layer 1 (top layer) and layer 2 (bottom layer); L_u, L_m and L_d are the upstream lip, mid lip and downstream lip lengths, respectively; $L_{f,1}$ and $L_{f,2}$ are the width of feed slot for top and bottom liquids. Like other pre-metred coating, the flow rate for both layers is the product of the wet thickness and web speed: $q_1 = h_{w,1} U_w$ and $q_2 = h_{w,2} U_w$.

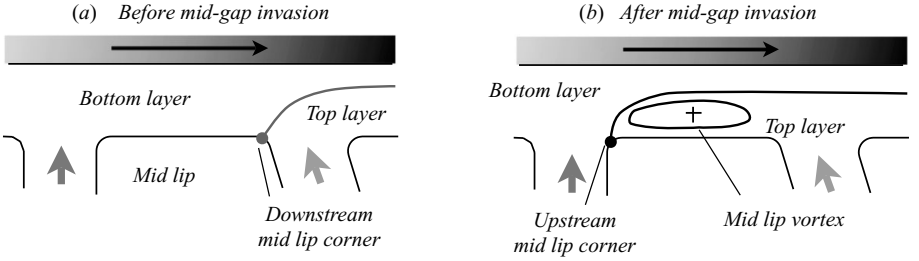

FIGURE 2. Sketch of inter-layer configuration before and after mid-gap invasion.

Several products require more than one layer for optimal performance. The most efficient way to manufacture these products is by coating all the layers at once before they are solidified. Slot coating process can be easily adapted for coating two different layers as shown in figure 1.

The coating die has two separate feed slots through which each layer is fed. The flow can be divided into three regions separated by the feed slots: upstream gap, mid gap and downstream gap. When both liquids are immiscible, they form an inter-layer inside the coating bead. But, in several coating applications, both layers use solvents that are miscible, and the apparent interface is truly an inter-diffusion zone. However, because of the relatively high speed of the moving web (typically about $1\,\mathrm{m\,s^{-1}}$) and the small length of die lip ($\sim$1 mm), the residence time in the coating bead is extremely small and so is the thickness of the diffusion zone (Musson 2001): it is so thin that it can be considered as a distinct inter-layer with zero interfacial tension.

The inter-layer starts at the separation point (or line, in three dimensions), located somewhere in the mid die block. The point usually lodges on the downstream corner of the mid lip (figure 2*a*), but it can transit from one corner to the other, as observed by Cohen (1993), as operating condition changes. Thus the inter-layer and the top

liquid layer can invade the mid gap region, accompanied by dangerous turn-around flow and sometimes by the appearance of microvortex (figure 2*b*), as reported by Cohen (1993), Sartor *et al.* (1999) and Musson (2001).

This microvortex is deleterious, because it may create a mixing zone between both layers, which will spoil the functionality of the final product. Wilson *et al.* (2006) discussed how fluid recirculating for a long time in coating flows causes coating defects and stirring. The microvortex also may become nodular along their length and spoil the transverse uniformity of the inter-layer, which is also critical, especially in optical products. Moreover, as will be shown in this study, when the separation line is not located at the downstream corner of the mid die lip, its location is very sensitive to process conditions, leading to downweb variation on the coated layer, also compromising the final-product quality. The observed oscillation may indicate the presence of multiple solutions or that a steady flow state does not exist. Armi (1986) has shown that for two-layer flows through contractions, there are two distinct solutions.

Therefore, as discussed by Sartor *et al.* (1999), the ideal location of the separation point that leads to the desired steady flow is the downstream corner of the mid die lip, as shown in figure 2(*a*). The movement of the separation point from its desired location along the mid die lip is usually referred to as mid-gap invasion, and its occurrence can be associated with the onset of coating defects. It is crucial to determine the set of process conditions at which it happens.

Here, we analyse mid-gap invasion by flow visualization and by the solution of the two-dimensional Navier–Stokes equation for free-boundary flows. Through both approaches, we determined the critical operating conditions at the onset of mid-gap invasion and the different mechanisms behind it. We realized that an approximate and simple criterion that defines the occurrence of mid-gap invasion can be derived using lubrication approximation. The reported results define the operability limits of two-layer slot-coating flows related to inter-layer uniformity.

2. Mid-gap invasion: flow visualization

Since mid-gap invasion is related to the movement of the inter-layer as process conditions change, we visualized its location inside a dual slot-coating flow as a function of flow parameters and liquid properties in order to determine the critical conditions at which mid-gap invasion occurs.

2.1. *Experimental set-up*

The bench-scale experiment coater, specially designed to visualize coating flows used in these experiment, is shown in figure 3.

The coating solutions were stored in two separated tanks which were connected to calibrated precision gear pumps (Parker-Nichols Zenith, West Newton, MA, USA). We installed filters (model type 54/95, Balston Corp., Haverhill, MA, USA) between the tanks and the pumps to prevent any residual particle from entering into the pumps. Both flow rates were controlled by the pump speed and measured with a Coriolis flow metre (model MFC 100/MFS 3000, Krohne America Inc., Peabody, MA, USA). Downstream of both pumps, the liquid flows through a debubbler (Whitey 12FK088 304L-HOF4-1000cc, Swagelok Co., Solon, OH, USA) in order to eliminate any small bubble inside the liquid and to dampen pulsations from the pumps. Both coating liquids were fed to two separate cavities of the 4 inch wide stainless steel coating die. Inside the cavities, liquid is distributed along the width of the die and

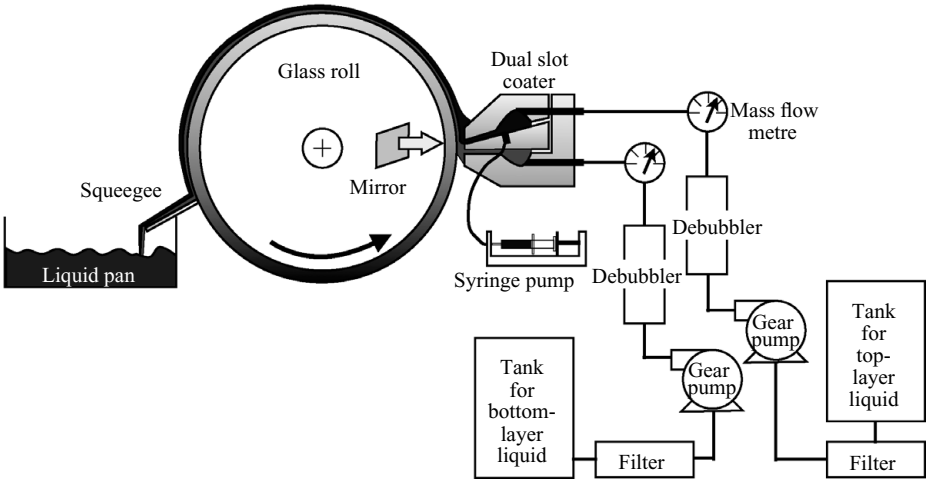

FIGURE 3. Schematic of the experimental dual slot-coating apparatus. Camera is installed parallel to the axis of the roll such that it can visualize the coating bead through the glass roll by focusing in a mirror mounted at a 45° angle.

flows through a narrow feed slot. The feed-slot heights were set to 250 μm by shims. The die was mounted such that the gap between the die and the roll was easily adjusted. As indicated in figure 3, the downstream die lip formed a slightly converging channel with the roll surface, with an inclination angle of $\theta_l = 5°$. Both liquids were coated as a two-layer flow on to an 8 inch in diameter high-quality optical glass roll (Professional Instruments, Hopkins, MN, USA). The speed of the roll surface could be controlled from 7 m min^{-1} up to 20 m min^{-1}. Because no substrate was used, the coated liquid, except a trace residue, was removed from the roll surface by a Teflon squeegee. The used coating liquids were solutions of water and glycerine. Two different concentrations of glycerine solution were used (73 % and 80% by weight) so that the viscosity could be changed from 28.5 cP to 57.0 cP. The viscosity of the Newtonian solution was measured with a Brookfield viscometer (YULA-15 ULA Spindle, Model DV-II+, Brookfield Engng Lab., Stoughton, MA, USA).

Since both coating liquids are transparent, the inter-layer was marked by the dark blue dye (FD&C Blue No.1 food grade dye, Fischer United Supply Co., Minneapolis, MN, USA) which was mixed with top-layer coating liquid and injected by a syringe pump (model 230, KD Scientific, Holliston, MA, USA) through a small port in mid die block shoulder.

A video camera (model NX18A, NEC, Tokyo, Japan) with microscope lens (Magnazoom 6000 with 0.5× adapter, Navitar, Rochester, NY, USA) was focused on a right-angle mirror mounted inside the open end of the roll in order to visualize the flow in the coating bead through the glass wall as in figure 3. The inter-layer separation-line position could be marked by the end of the dye streakline in this view as sketched in figure 4. If the streakline only appeared downstream of the mid die lip, the separation point was located at the desired location, and mid-gap invasion did not occur. After the onset of mid-gap invasion, the blue die was clearly observed under the mid lip, as shown in figure 4. The circular and transverse motion of the streakline is a definite evidence of the presence of the undesired microvortex under the mid lip, as was also observed by Cohen (1993).

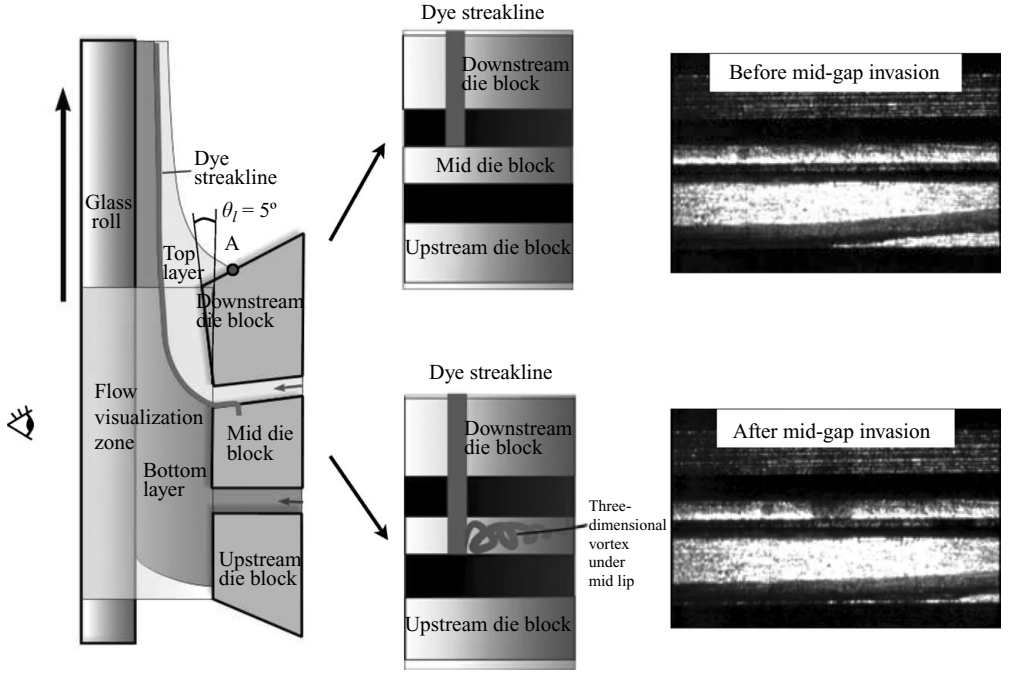

FIGURE 4. Flow visualization of mid-gap invasion thorough the glass roll. Inter-layer is marked by a colour dye. Inter-layer movement and evidence of microvortex at the mid lip were captured by the location of dye streakline. Near the critical mid-gap invasion conditions, inter-layer oscillates along the mid lip.

2.2. *Onset of mid-gap invasion*

The onset of mid-gap invasion was determined at different gaps $H_g = 210$, 260 and 360 μm and viscosity ratios $m = \mu_1/\mu_2 = 0.5$, 1 and 2, where μ_1 and μ_2 are the viscosity of the top and bottom layers, respectively. The goal was to find the values of coating thickness (flow rate) of both layers at which mid-gap invasion occurs. The critical conditions were found by the following procedure: First, the roll speed and flow rate of each layer were adjusted such that the separation line was located at the downstream corner of the mid lip; i.e. at these conditions mid-gap invasion was not observed. Then, one of the three operating parameters, top-layer flow rate, bottom-layer flow rate and roll speed, was slowly varied, keeping the others constant. After each step change, we waited at least 1 min to reach a new steady state before recording the position of the separation point.

Mid-gap invasion was not observed while changing the top-layer flow rate for all gaps, and viscosity were ratios explored. As the top-layer flow rate rose, the static contact line at the downstream free surface (point A in figure 4) moved along the downstream die shoulder, and the separation point remained at the downstream corner of the mid lip. Mid-gap invasion was only observed when lowering the bottom-layer flow rate or raising the roll speed, from the initial set of parameters. Near the critical conditions for mid-gap invasion, the inter-layer position oscillated. Even with all the operating parameters fixed, dye streaklines under the mid lip appeared and disappeared periodically. We suspect that at these conditions, the position of the separation line is extremely sensitive to flow parameters and the small oscillations on flow rate, due to the gear pump, the and gap, due to roll run-out, is enough to cause

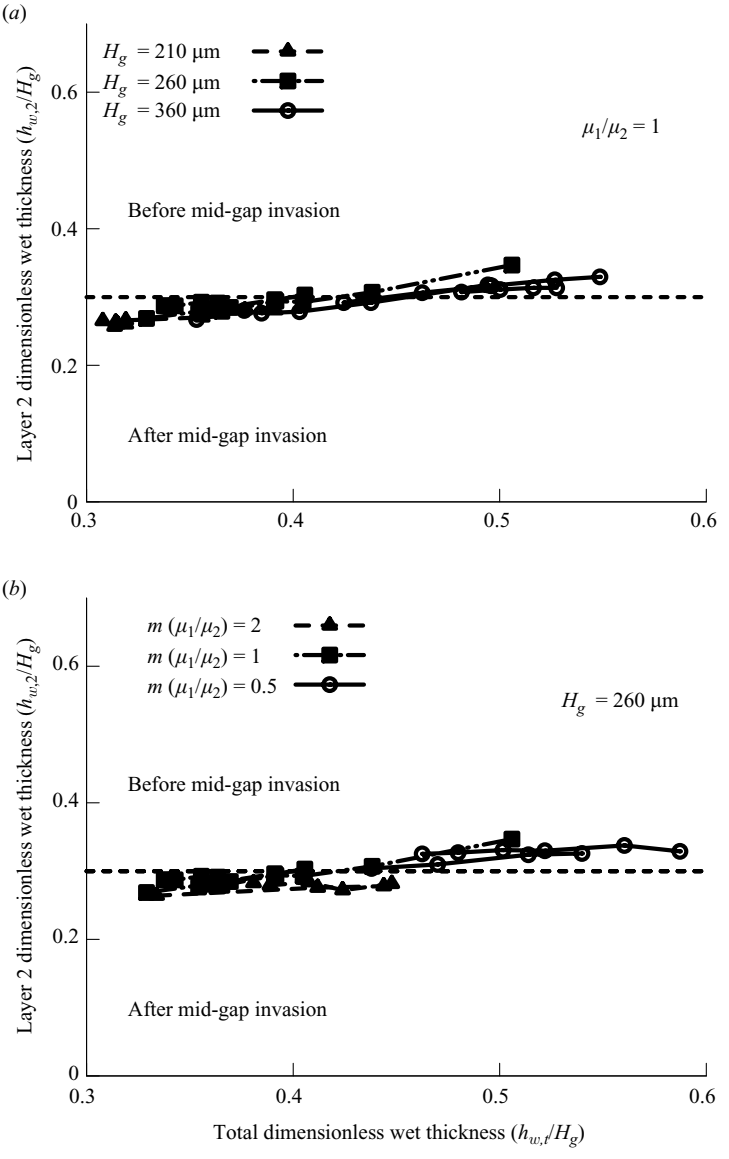

FIGURE 5. Critical bottom-layer thickness at mid-gap invasion as a function of the total wet thickness, gap height (*a*) and viscosity ratio (*b*).

the observed behaviour. We considered the critical condition at the onset of mid-gap invasion the set of parameters at which the oscillation of the separation point could be observed.

The results show that the parameter that determines the mid-gap invasion is the bottom-layer wet thickness $h_{w,2}$, which can be varied by changing both the pump rotation and the roll speed. Figure 5(*a*) shows the critical bottom-layer thickness in units of coating gap $h^*_{w,2} = h_{w,2}/H_g$ at which mid-gap invasion occurred as a function of the total thickness $h^*_{w,t} = h_{w,t}/H_g = (h_{w,1} + h_{w,2})/H_g$ at different gaps, and figure 5(*b*) shows viscosity ratios. The curves at different gaps and viscosity ratios fall on top of each other, showing that these parameters do not affect the critical value

of $h^*_{w,2}$. Moreover, the effect of the total thickness is extremely weak. At small values of the total wet thickness, e.g. $h_{w,t}/H_g \approx 0.3$, the critical dimensionless bottom layer is approximately $h^*_{w,2} \approx 0.26$; at large total thickness, e.g. $h_{w,t}/H_g \approx 0.55$, the critical value is $h^*_{w,2} \approx 0.34$.

In summary, the experimental results show that the bottom-layer thickness in units of gap is the key operating parameter that triggers mid-gap invasion. The critical condition is a function of the bottom-layer flow rate q_2, web speed U_w and coating gap H_g ($h^*_{w,2} = q_2/(H_g\, U_w)$), and it is independent of liquid properties. The results also show that near the critical condition, the separation line oscillates along the mid lip. The mechanism that drives this phenomenon and the evolution of flow states were examined here by solving the Navier–Stokes equation.

3. Mid-gap invasion: Navier–Stokes theory

The flow in coating bead is described by the complete two-dimensional, steady-state mass and momentum conservation equations for free-surface flows. Here, there are three free boundaries, the upstream and downstream gas–liquid interfaces and inter-layer between the two liquids. The goal of the numerical analysis is to determine the inter-layer configuration as a function of the flow parameters and consequently determine numerically the onset of mid-gap invasion. In order to allow inter-layer movement along the die lip surface, the edges of the coating die were described as rounded corners with prescribed radius of curvature, which are usually set by limitations on the machining process (Romero, Scriven & Carvalho 2006). Here, we changed the bottom-layer flow rate, keeping the top-layer flow rate constant at different viscosity ratios.

3.1. *Governing equation and boundary conditions*

The velocity and pressure fields of incompressible two-dimensional, steady-state flow of a Newtonian liquid are governed by the continuity and momentum equations:

$$\nabla \cdot \boldsymbol{u} = 0, \quad \rho_i\, \boldsymbol{u} \cdot \nabla \boldsymbol{u} = \nabla \cdot \boldsymbol{T}_i, \tag{3.1}$$

where ρ_i is the liquid density and $\boldsymbol{T}_i$ is the stress tensor. For Newtonian liquid, it is given by $\boldsymbol{T}_i = -p\boldsymbol{I} + \mu_i[\nabla \boldsymbol{u} + (\nabla \boldsymbol{u})^T]$, where $\boldsymbol{I}$ is the identity tensor, p the pressure and μ_i the liquid viscosity. Here, subscript i defines the two liquid phases, $i = 1$ for the top layer and 2 for the bottom layer.

Boundary conditions are needed to solve the Navier–Stokes system. In a two-layer slot-coating flow, the domain is bounded by inflow and outflow planes, solid walls and free surfaces (gas–liquid interfaces) and the surface that separates the two liquids, the inter-layer, as shown in figure 6. To simplify the geometry, we considered the downstream die lip parallel to the moving web in the numerical analysis. We verified that this small change in the geometry of the downstream die lip does not affect the critical condition at the onset of mid-gap invasion by comparing the predictions obtained with both configurations.

At the inflow planes, we imposed

$$\boldsymbol{u} = \boldsymbol{U}_b(\boldsymbol{x}), \tag{3.2}$$

where $\boldsymbol{U}_b(\boldsymbol{x})$ is the imposed parabolic velocity profile. At the outflow plane we impose

$$\boldsymbol{n}_b \cdot \nabla \boldsymbol{u} = 0, \tag{3.3}$$

$$p = p_b, \tag{3.4}$$

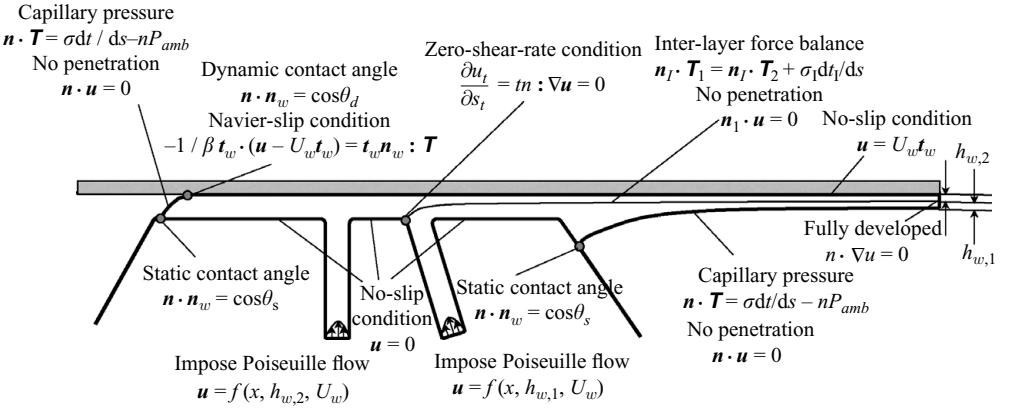

FIGURE 6. Boundary conditions used for two-layer dual slot-coating flow model. Free-surface and inter-layer configurations are unknown and part of the solution.

where p_b is the imposed outflow pressure (ambient pressure) and $\boldsymbol{n}_b$ is the unit normal vector to the boundary. The total wet thickness $h_{w,t}=h_{w,1}+h_{w,2}$ is determined by the flow rate of each layer and the web velocity U_w. The outflow plane was located a distance equal to $10\,H_g$ downstream of the die corner. Moving the outflow plane in the downstream direction did not affect the free-surface configuration. At rigid solid walls, the no-slip and no-penetration boundary conditions were imposed. Along the web,

$$\boldsymbol{t}_w\cdot\boldsymbol{u}=U_w,\quad \boldsymbol{n}_w\cdot\boldsymbol{u}=0, \tag{3.5}$$

where U_w is the solid wall velocity and $\boldsymbol{n}_w$ and $\boldsymbol{t}_w$ are the vectors unit normal and tangent to the wall. Along the die surface, $\boldsymbol{t}_w\cdot\boldsymbol{u}=0$ and $\boldsymbol{n}_w\cdot\boldsymbol{u}=0$. At the dynamic contact point, where the upstream meniscus meets the moving web, Navier-slip condition is used instead of no-slip condition,

$$\frac{1}{\beta}\boldsymbol{t}_w\cdot(\boldsymbol{u}-U_w\boldsymbol{t}_w)=\boldsymbol{t}_w\boldsymbol{n}_w:\boldsymbol{T}, \tag{3.6}$$

where β is slip coefficient. Here we choose $\beta=0.1\,\mathrm{g}^{-1}\,\mathrm{s}^{-1}$, based on the numerical tests reported by Sartor (1990).

Along the gas–liquid interfaces, a force balance and the no-penetration condition (kinematic condition) were imposed:

$$\boldsymbol{n}_f\cdot\boldsymbol{T}_i=\sigma\frac{\mathrm{d}\,\boldsymbol{t}_f}{\mathrm{d}\,s}-\boldsymbol{n}_f\,P_{amb}, \tag{3.7}$$

$$\boldsymbol{n}_f\cdot\boldsymbol{u}=0, \tag{3.8}$$

where $\boldsymbol{t}_f$ and $\boldsymbol{n}_f$ are the vectors locally unit tangent and normal to the free surface; s is the arclength coordinate along the interface; σ is the liquid surface tension; and P_{amb} is the ambient pressure.

Like the gas–liquid interfaces, the position of the inter-layer is unknown *a priori*. In order to track its location, three conditions – force balance, no-penetration and velocity continuity – are to be satisfied along the inter-layer:

$$\boldsymbol{n}_I\cdot\boldsymbol{T}_1=\boldsymbol{n}_I\cdot\boldsymbol{T}_2+\sigma_I\frac{\mathrm{d}\,\boldsymbol{t}_I}{\mathrm{d}\,s}, \tag{3.9}$$

$$\boldsymbol{n}_I\cdot\boldsymbol{u}_1=\boldsymbol{n}_I\cdot\boldsymbol{u}_2=0, \tag{3.10}$$

$$\boldsymbol{t}_I\cdot\boldsymbol{u}_1=\boldsymbol{t}_I\cdot\boldsymbol{u}_2, \tag{3.11}$$

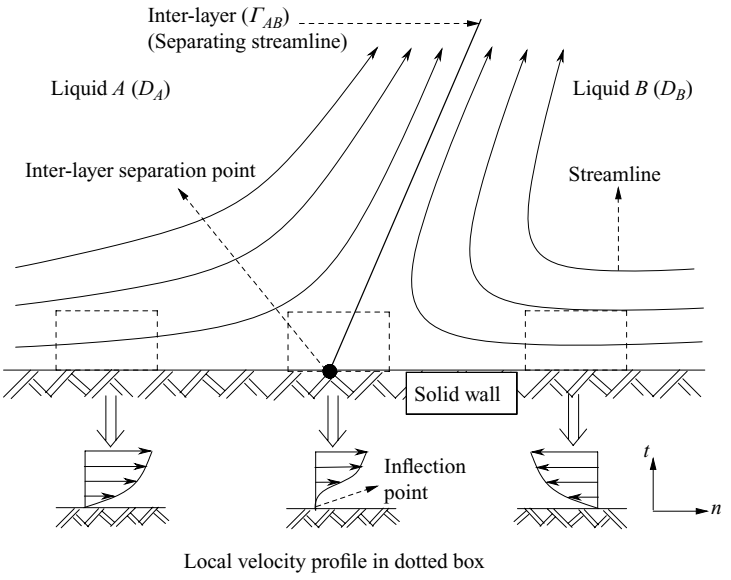

FIGURE 7. Flow near inter-layer separation point at the solid wall. The local velocity profiles near the wall at different locations around the separation point are shown in the dotted boxes. The inflection point of the velocity profile is the indication of zero shear rate at the inter-layer separation point.

where $\boldsymbol{n}_I$ and $\boldsymbol{t}_I$ are the vectors unit normal and tangent to the inter-layer; $\boldsymbol{u}_i$ and $\boldsymbol{T}_i$ are velocity and stress tensor for phase i; and σ_I is the interfacial tension.

The singularity of the stress field at a static inter-layer separation point is integrable; e.g. the total shear force on the wall is finite (Silliman & Scriven 1980). Therefore, there is no need to relieve the stress singularity, and the no-slip condition is acceptable. An extra condition is needed to set the location of the separation point.

The inter-layer separation point is nothing more than a regular *separation point* on a solid wall, except that liquids are different on either side of the inter-layer, which is just a 'special' dividing or separating streamline. Because of the flow reversal at the separation point, the profile of the tangent velocity presents an inflection point, as sketches in figure 7 (Schlichting & Gersten 2001):

$$\frac{\partial u_t}{\partial s_n} = 0, \tag{3.12}$$

where u_t is the tangential velocity component and s_n is the arclength coordinate normal to the wall.

Because the velocity along the wall is zero, $\partial u_t/\partial s_t = 0$ (s_t is the arclength coordinate along the wall). Therefore, the normal deformation rates at the separation point vanish. For Newtonian liquids, vanishing deformation rate is equivalent to vanishing viscous stress. The force balance condition (3.9) at the separation point reduces to the well-known *Young–Laplace equation*:

$$p_1 = p_2 + \sigma_I \left(\boldsymbol{n}_I \cdot \frac{\mathrm{d}\, \boldsymbol{t}_I}{\mathrm{d}\, s} \right) = p_2 + \sigma_I (2H), \tag{3.13}$$

where H is the mean curvature of the interface at the separation point. Furthermore, when the interfacial tension is negligible, one may find that this equation boils down

to the *equal pressure* condition:

$$p_1 = p_2. \tag{3.14}$$

This is the condition used by Scanlan (1990) and Musson (2001) to track the inter-layer separation point with zero interfacial tension.

Here we use the more general zero-shear-rate condition as a boundary condition for the mesh equations in order to track the inter-layer separation point along the mid lip. All boundary conditions are summarized in figure 6.

Flows with free surfaces and inter-layer give rise to a *free-boundary problem*. The flow domain is unknown *a priori*, and it is part of the solution.

To solve a free-boundary problem by means of standard techniques for boundary-value problems, the set of differential equations and boundary conditions posed in the unknown physical domain have to be transformed to an equivalent set defined in a known, fixed computational domain. This transformation is made by a mapping $\boldsymbol{x} = \boldsymbol{x}(\boldsymbol{\xi})$ that connects the two domains. The physical domain is parameterized by the position vector $\boldsymbol{x} = (x, y)$ and the reference domain by $\boldsymbol{\xi} = (\xi, \eta)$. The mapping used here is the one described by de Santos (1991). The inverse mapping is governed by a system of elliptic differential equations identical to those encountered in the dilute regime of diffusional transport,

$$\nabla \cdot D_\xi(\xi, \eta)\nabla\xi = 0, \quad \nabla \cdot D_\eta(\xi, \eta)\nabla\eta = 0, \tag{3.15}$$

where D_ξ and D_η are mesh diffusivities which control the steepness of gradients in the node spacing by adjusting the potentials ξ and η. Curves of constant ξ and η define the boundaries of elements used to describe the domain. The cross-point of these curves sets the position of a node. Boundary conditions are needed to solve the second-order differential equations (3.15). Solid walls and inflow and outflow planes are described by the function that defines their geometry, and nodes were distributed along them by a specified stretching function. The location of the free surfaces and inter-layer are implicitly determined by the corresponding kinematic conditions, (3.8) and (3.10). The discrete version of the mapping equations is generally referred to as mesh-generation equations. Detailed procedure and boundary conditions for mesh equation are discussed in de Santos (1991).

3.2. *Solution of the Navier–Stokes system for free-surface flow by Galerkin finite element method*

Galerkin finite element method (G/FEM) is used to solve the Navier–Stokes system (3.1) coupled with the mesh-generation equation (3.15). Each independent variable, velocity, pressure and nodal position, is approximated by a linear combination of a finite number of basis functions, which are the unknowns of the discretized problem. The velocity and nodal position are represented in terms of Lagrangian biquadratic function $\phi^i(\xi, \eta)$ and the pressure in terms of linear discontinuous basis function $\psi^k(\xi, \eta)$.

This particular choice of basis functions have two advantages in dealing with the inter-layer. The choice of the biquadratic function for velocity requires sharing velocity nodal point between both layers along the inter-layer. Therefore velocity continuity is redundant, and only the no-penetration along the inter-layer needs to be imposed. The other merit comes from the discontinuous pressure field. Pressure jump can occur across the inter-layer (Mavridis, Hrymak & Vlachopoulos 1987), even in the absence of interfacial tension. The linear discontinuous basis function can handle the jump naturally without any modification, as was needed to be done by Mavridis *et al.* (1987) and Scanlan (1990).

The weak forms of (3.1) and (3.15) are obtained by multiplying each equation by weighting functions, integrating over the physical domain and applying the divergence theorem to the appropriate terms. Essential boundary conditions were imposed by replacing the corresponding weighted residual equation with the desired velocity or node specification. Natural boundary conditions were applied through the boundary integrals that come from the divergence theorem.

In sum, the G/FEM reduces the Navier–Stokes and mesh-generation differential equations to a set of nonlinear algebraic equations on the basis function coefficients,

$$\boldsymbol{R}(z, \boldsymbol{\lambda}) = 0, \tag{3.16}$$

where z is the solution vector which consists of the finite element coefficients for velocity $\boldsymbol{u}$, pressure P and position $\boldsymbol{x}$, and $\boldsymbol{\lambda}$ is a vector that contains the parameters on which the system depends; (3.16) is solved iteratively by Newton's method:

$$\begin{gathered} \boldsymbol{J}^{(i)}\left(z^{(i)}, \boldsymbol{\lambda}\right) \delta z^{(i)} = -\boldsymbol{R}^{(i)}\left(z^{(i)}, \boldsymbol{\lambda}\right), \\ z^{(i+1)} = z^{(i)} + \delta z^{(i)}, \end{gathered} \tag{3.17}$$

where the indices i and $i+1$ indicate the current and next Newton's step and $\boldsymbol{J}^{(i)} \equiv \partial \boldsymbol{R}^{(i)}/\partial z^{(i)}$ is the Jacobian matrix. The iteration continues until $\|\boldsymbol{R}^{(i)}\|_2 < \epsilon$. Here we choose $\epsilon = 10^{-8}$.

3.3. *Designing a mesh to track the inter-layer separation point*

In order to study numerically the mid-gap invasion phenomenon with the approach described here and to determine the flow parameters at which the inter-layer separation point moves along the mid die lip, special care is required to design the free-boundary-conforming mesh used to descretize the domain. Previous works on two-layer slot coating that used similar approach did not focus on mid-gap invasion phenomenon (Scanlan 1990; Musson 2001). Taylor & Hrymak (1999) determined the interface zone by using a fixed mesh with convection–diffusion equation for imaginary tracer species, with arbitrarily chosen tracer diffusivity, not requiring special care with the mesh near the separation.

Because the model needs to capture the movement of the separation point, the die edges cannot be described as mathematical corners, which would lead to an artificial pinning of the inter-layer separation point. We describe the lip geometry as a combination of lines and arc of circles. The radius of curvature of each die corner was set to 50 μm. In order to describe the lip geometry accurately, the mesh needs to be concentrated along the sections of the curve that corresponds to the arc of circle, i.e. the die corner. One possibility is to distribute the modes along the die surface using a weighting function (Thompson, Warsi & Mastin 1985) based on the curvature of the domain boundary:

$$w(s) = 1 + \alpha|\kappa(s)|, \tag{3.18}$$

where s is the arclength coordinate along the boundary; $\kappa(s)$ is curvature; and α is user-defined coefficient to adjust the concentration of the nodes.

The use of this function was not effective, since the curvature is discontinuous at the point at which the straight line and arc of circle meet, leading to large gradients on the elements near that point.

To prevent the discontinuity on the weighting function $w(s)$, which may cause discretization error, a modified function $w_s(s)$, with continuous derivative, was used instead. It was constructed by solving the time evolution of a diffusion-like process

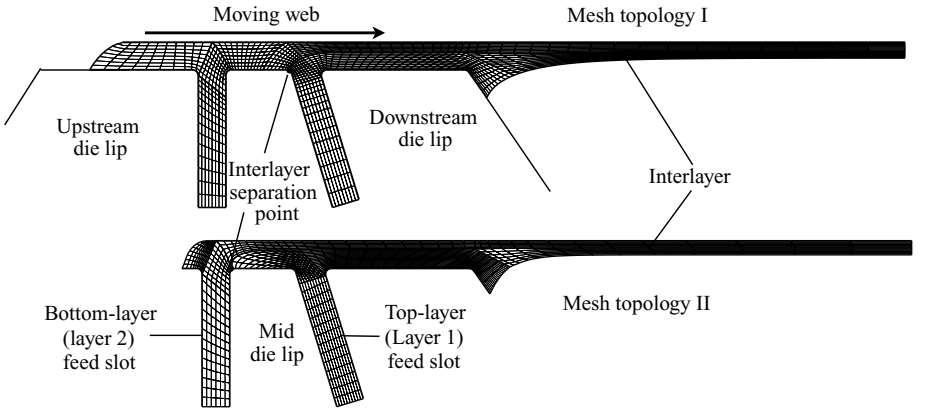

FIGURE 8. Two mesh topologies for the mid-gap invasion. Mesh topology I provides less distorted mesh when the inter-layer separation point is close to downstream corner of the mid lip, i.e. before mid-gap invasion flow state. Mesh topology II is suitable when the point is near upstream corner of the mid lip, i.e. after mid-gap invasion flow state.

using $w(s)$ as the initial condition:

$$\left.\begin{aligned} \frac{\partial w^*}{\partial t} &= \frac{\partial^2 w^*}{\partial s^2}, \\ w^*(t=0,s) &= w(s). \end{aligned}\right\} \tag{3.19}$$

The weighting function used to distribute the nodes along the die wall $w_s(s)$ was the solution of (3.19) at an arbitrary time $t = t^*$:

$$w_s(s) = w^*(t^*, s). \tag{3.20}$$

The degree of smoothness increases with t^*. Here, we chose $t^* = 0.01$. The weighting functions constructed this way are compatible with the hyperbolic-tangent stretching functions used by Vinokur (1983), and they were adequate to construct finite element meshes that allowed an accurate representation of the die surface, including the rounded corners.

Because of the large mesh deformation that occurs as the separation point moves upstream along the die lip, we used two different mesh topologies, one designed for flow states before the mid-gap invasion occurred (I) and the other designed for flow states after the mid-gap invasion (II). Figure 8 illustrates both mesh topologies. Mesh I had 1392 elements and the resulting nonlinear system along with 27508 degrees of freedom, whereas mesh II had 1068 elements and 21 128 degrees of freedom. For each mesh configuration, solutions with different discretizations were also obtained at $\mu_1/\mu_2 = 1$. The solution paths obtained in the range tested did not change as the number of degree of freedom was raised to 30 128 in mesh I and 23 864 in mesh II.

3.4. *Results from numerical model: two mechanisms behind mid-gap invasion*

We present the evolution of the flow states as the bottom-layer thickness varies at different viscosity ratios. All the other operating and geometric parameters were kept fixed, and their values are presented in table 1. Experiments have shown that mid-gap invasion occurs at $h^*_{w,2} = h_{w,2}/H_g \approx 0.3$, so we chose two different solution paths for each viscosity ratio $m = \mu_1/\mu_2$ explored:

(*a*) With mesh I, start solution path at $h^*_{w,2} = 0.4$. Use arclength continuation by decreasing $h^*_{w,2}$.

Operating parameters

Name	Unit	Base case
Top-layer film thickness ($h_{w,1}$)	mm	0.0625
Web speed (U_w)	m s^{-1}	1
Ambient pressure (P_{amb})	Pa	0
Surface tension (σ)	dyne cm^{-1}	61
Interfacial tension (σ_I)	dyne cm^{-1}	0 or 1
Density ($\rho_1 = \rho_2$)	g cm^{-3}	1.2
Viscosity (μ_1 or μ_2)	cP	23 or 46 or 115
Dynamic contact angle (θ_d)	deg.	128
Static contact angle (θ_s)	deg.	62

Geometry parameters (see figure 1)

Name	Unit	Base case
Gap height (H_g)	mm	0.250
Upstream lip length (L_u)	mm	1.75
Mid lip length (L_u)	mm	0.500
Downstream lip length (L_d)	mm	1.25
Top-layer feed-slot width ($L_{f,1}$)	mm	0.250
Bottom-layer feed-slot width ($L_{f,2}$)	mm	0.250

TABLE 1. Parameters used in two-layer dual slot coating.

(*b*) With mesh II, start solution path at $h^*_{w,2} \lesssim 0.2$. (The actual value is a function of the viscosity ratio.) Use arclength continuation by raising $h^*_{w,2}$.

It is important to note that because the separation-point location is extremely sensitive to bottom-layer flow rate, the solutions presented here could not be computed by zeroth- or first-order continuation. Arclength continuation (Bolstad & Keller 1986) proved to be essential.

The location of the inter-layer separation point at zero interfacial tension ($\sigma_I = 0$) was recorded at different dimensionless bottom-layer flow rates $h^*_{w,2}$ at viscosity ratios $m =$ 0.2, 0.5, 1, 2 and 5. The results are presented in figures 9 and 10. The position of the separation point is parameterized by an arclength coordinate system defined along the mid die piece. On this system, the upstream corner of the mid lip is at $1.50 < s < 1.58$, and the downstream corner is at $2.08 < s < 2.14$.

Figure 9 shows the results at viscosity ratio $m = 1$ ($\mu_1 = \mu_2 = 23$ cP). The top branch corresponds to solutions computed with mesh I. The separation point stays at the downstream corner of the die lip for $h^*_{w,2} \gtrsim 0.33$. Below this value, its location becomes extremely sensitive to $h^*_{w,2}$. The solution path ends at a termination point, beyond which solutions could not be computed. The bottom branch in the figure corresponds to solutions obtained with mesh II. At low bottom-layer thickness, e.g. $h^*_{w,2} < 0.3$, the separation point is located at the upstream die corner. At $h^*_{w,2} \approx 0.3$, it moves downstream as the bottom-layer thickness rises. Again, the solution path ends at a termination point beyond which solutions could not be obtained. Both solution branches do not connect, but they indicate the existence of multiple solutions at $h^*_{w,2} \approx 0.31$. The high sensitivity of the separation-point location to the flow rate and moreover the occurrence of multiple solutions may explain the oscillation observed in the experiments near the conditions at which mid-gap invasion occurs.

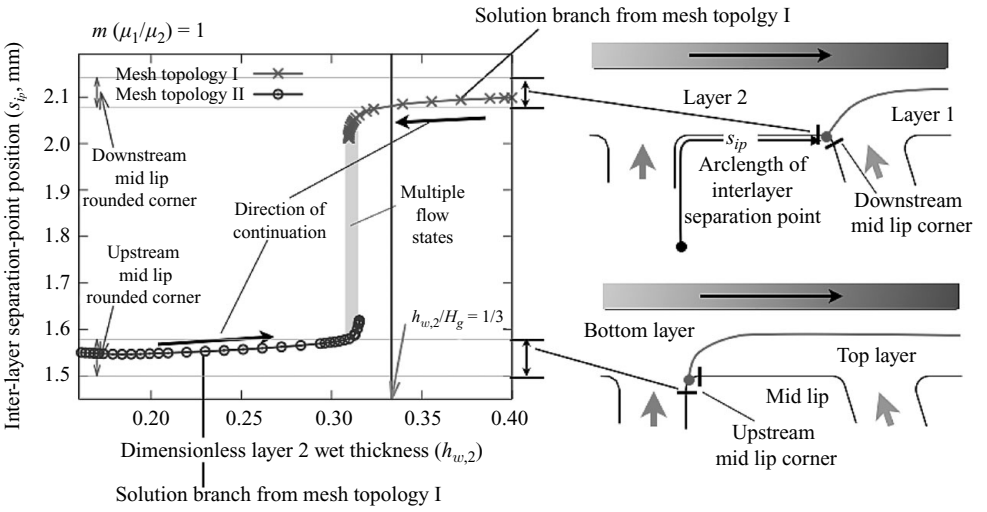

FIGURE 9. Inter-layer separation-point locations as functions of the dimensionless bottom-layer wet thickness for viscosity ratio $m = \mu_1/\mu_2 = 1$. For measurement of the inter-layer separation-point location, arclength along the mid die block was measured from the outflow boundary of bottom-layer (layer 2) inflow boundary. Note that in the shaded area near $h^*_{w,2} = 0.31$ both solution branches coexist, which implies possible multiple solutions for given flow rate.

The solution paths at different viscosity ratios are presented in figure 10. Clearly, the evolution of the inter-layer separation-point location as the bottom-layer dimensionless flow rate $h^*_{w,2}$ changes is different at low and high viscosity ratios. At high viscosity ratios ($m = 5$ and $m = 2$), solutions with the separation point located along the mid die lip could not be computed; the solution paths terminate at flow states at which the separation point is at the upstream or downstream corner of the mid lip. At low viscosity ratios ($m = 0.5$ and $m = 0.2$), flow states with the separation point at the mid lip could be computed. The curves resemble a typical hysteresis loop. At all viscosity ratios explored, there is a range of bottom-layer thickness at which multiple solutions existed. This range marks the onset of mid-gap invasion. Although the variation is small, the computed critical flow rate falls from $h^*_{w,2} \sim 0.34$ to $h^*_{w,2} \sim 0.2$ as the viscosity ratio rises from $m = 0.2$ to $m = 5$. The same behaviour was observed in the experiments shown in figure 5(b).

Snapshots of streamline plots at different dimensionless bottom-layer (layer 2) wet thickness $h^*_{w,2}$ along the solution branches at viscosity ratio $m = 0.2$ are shown in figure 11. At this low viscosity ratio, solutions with the inter-layer separation point from the downstream corner to the upstream corner of the mid lip could be computed with mesh topology I. At $h^*_{w,2} = 0.4$, the separation point is located at the downstream corner of the mid lip; the gap under the mid lip is filled only with liquid phase 2. As the bottom-layer thickness falls, the separation point moves upstream along the mid lip surface; its position is very sensitive to the $h^*_{w,2}$ in the range of $0.33 \lesssim h^*_{w,2} \lesssim 0.4$. The flow states at $h^*_{w,2} = 0.27$ computed with both meshes are virtually the same. The bottom flow branch is constructed by raising the flow with mesh topology II. In this case, the separation point departs from the corner only at $h^*_{w,2} > 0.35$, and it is clear that there are two different solutions at $h^*_{w,2} = 0.34$. The flow branches show that once

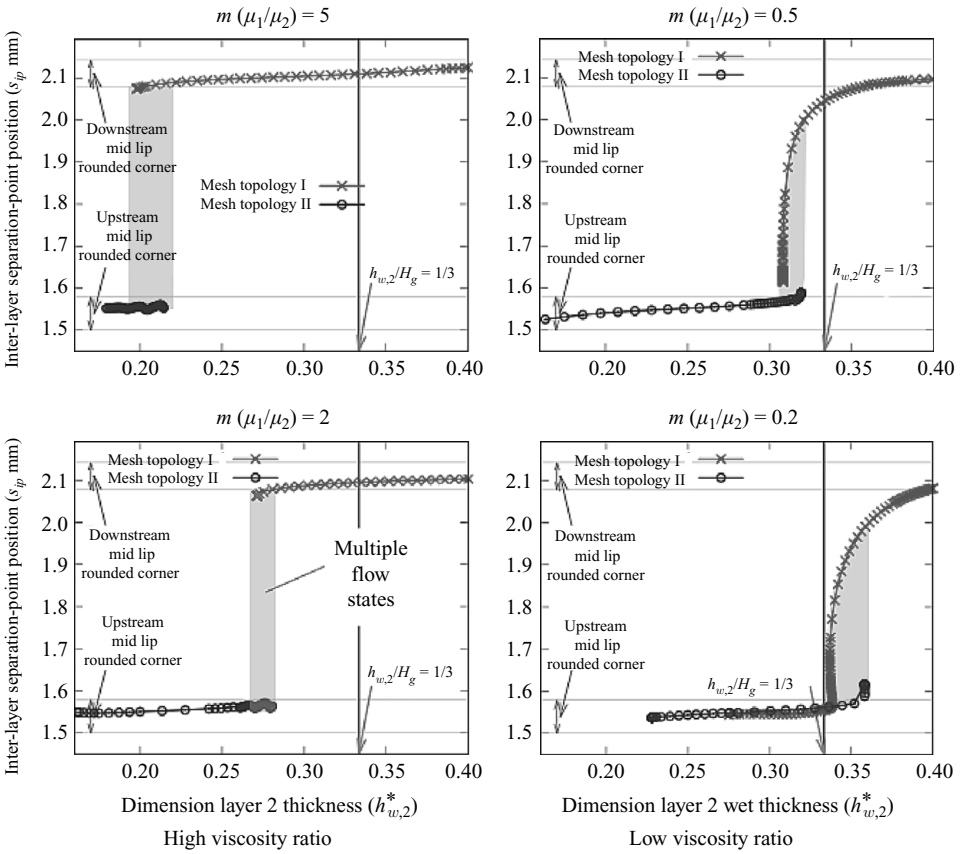

FIGURE 10. Inter-layer separation-point location as a function of the dimensionless bottom-layer wet thickness at viscosity ratio $m = 0.5$, 0.2, 2 and 5. For high viscosity ratio, $\mu_2 = 23$ cP and μ_1 is either 46 cP or 115 cP. For low viscosity ratio, $\mu_1 = 23$ cP and μ_2 is either 46 cP or 115 cP.

a separation point is located on a rounded corner with a small radius of curvature, it tends to stay there, leading to a hysteresis loop.

Figure 12 presents different flow states along the flow branches at high viscosity ratio, $m = 5$. The solution branch from mesh topology I shows that the inter-layer separation point does not move as $h^*_{w,2}$ falls. It is still located at the downstream corner even at $h^*_{w,2} \approx 0.2$. Because of the low bottom-layer flow rate, a microvortex attached to the die surface appears around $h^*_{w,2} = 0.33$. Its size grows rapidly as $h^*_{w,2}$ falls. The gap under the mid lip is filled with liquid phase 2 only.

The solution branch obtained with mesh topology II cannot go beyond $h^*_{w,2} = 0.215$ as $h^*_{w,2}$ rises. The cause of failure comes from the mesh distortion in the middle of inter-layer near the downstream corner: the inter-layer configuration approaches a cusp. There is clearly a region of multiple solution around $h^*_{w,2} = 0.2$. The different flow patterns at $h^*_{w,2} = 0.202$ are shown in the inserts of figure 12. Both flows show a large recirculation under the mid lip. The difference is that the separation point is located at different extremes of the lip. In the top branch, the vortex structure is filled with the bottom-layer liquid. In the bottom branch, the top layer has invaded the mid gap, and the recirculation is filled with liquid phase 1 (top layer).

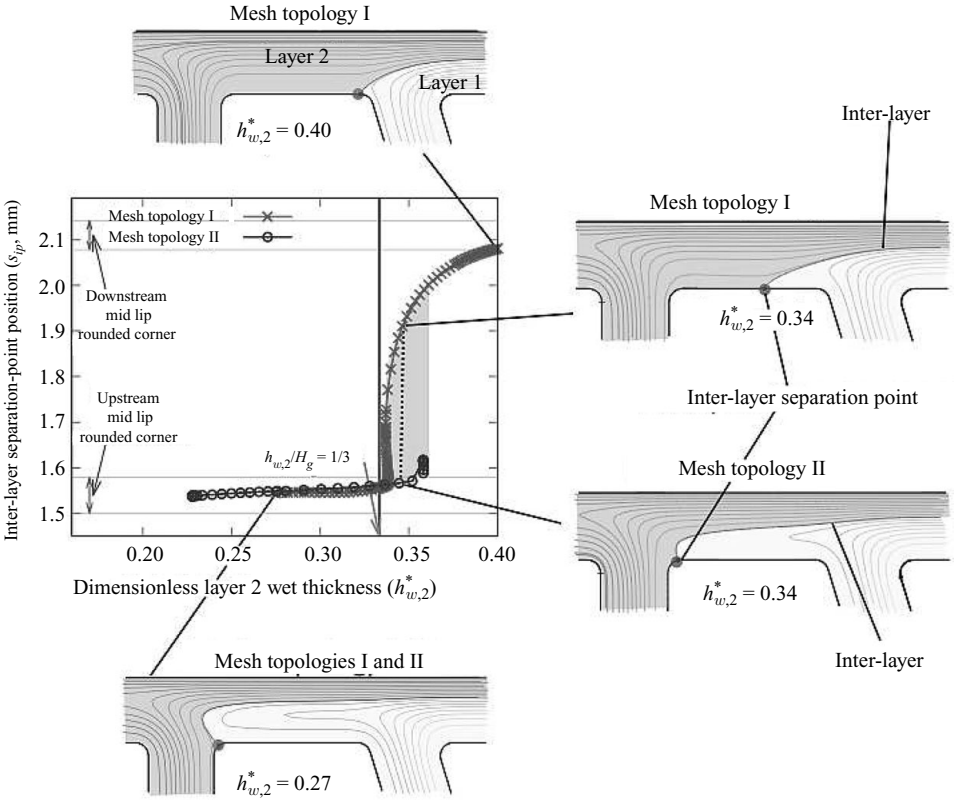

FIGURE 11. Inter-layer separation-point location as a function of the dimensionless bottom-layer wet thickness at viscosity ratio $m = 0.2$. Shaded area inside the plot indicates possible multiple solutions. Note that both mesh topology I and mesh topology II show the same streamline plots at $h^*_{w,2} = 0.27$.

Along the top branch, the recirculation of liquid phase 2 under the mid lip grows as the bottom-layer flow rate falls to a point at which the separation bubble almost touches the inter-layer, inside the dashed rounded box in the plot. Along the bottom branch, the recirculation of liquid phase 1 shrinks as the bottom-layer flow rate rises up to a point at which the inter-layer almost touches the saddle point of the streamline, located inside the dashed rounded box.

Since the model does not allow flow though the inter-layer, we cannot capture the mixing between two layers. However, these two different flow states at the same set of parameters strongly suggest that a mixing zone will be created after the streamline that defines the vortex touches the inter-layer or the saddle point. The evolution of the flow states resembles the birth of the saddle point inside a flow which is accompanied by the formation of cusp point on the separating streamline. The inter-layer separation point jumps to the upstream corner of the mid lip. Therefore the oscillation of the inter-layer observed during the experiments can be explained by the oscillation between the two flow states with the formation of a mixing zone.

The results show that the evolution of flow states as the bottom-layer flow rate falls and mid-gap invasion occurs at low viscosity ratio is different from that at high viscosity ratio. This difference is summarized in figure 13. When the top layer is less viscous than the bottom layer (low viscosity ratio), the separation point travels

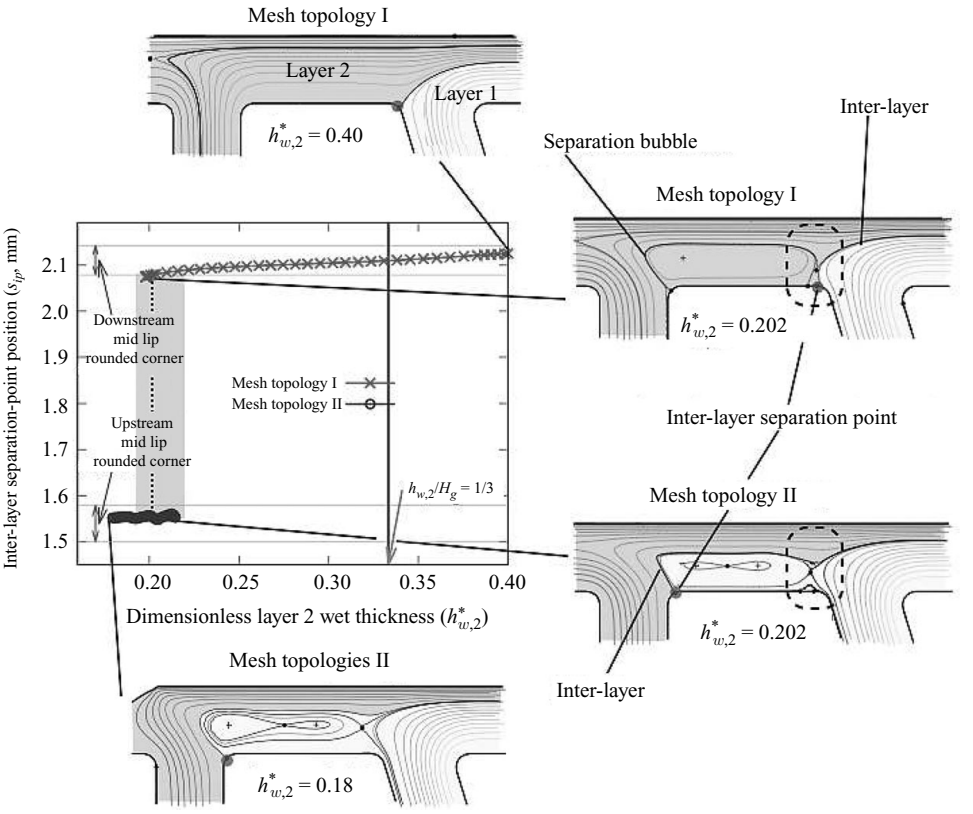

FIGURE 12. Plot of inter-layer separation point with respect to the dimensionless bottom-layer wet thickness for viscosity ratio $m = 5$. Note that there are two different flow states at $h^*_{w,2} = 0.202$. For the mesh topology I solution, dashed rounded box shows the area in which the inter-layer touches the microvortex. For the mesh topology II solution, dashed rounded box shows the area in which the saddle point of streamline is located.

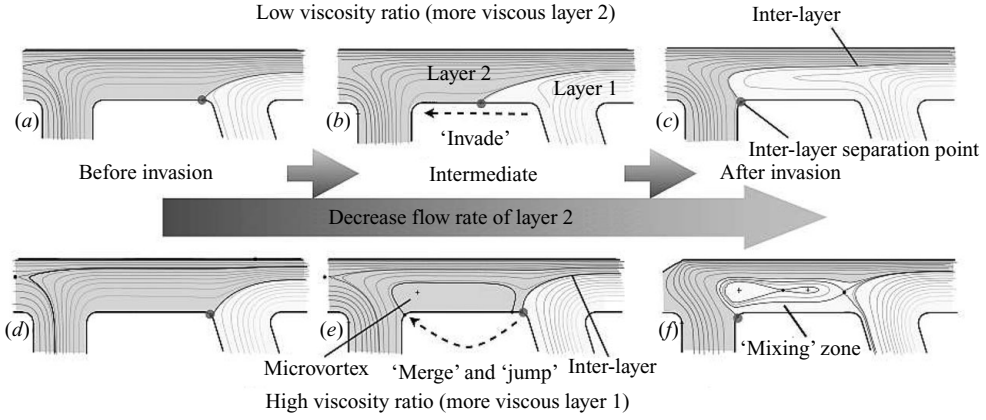

FIGURE 13. Two mechanisms of mid-gap invasion. In these plots, low viscosity ratio corresponds to $m = 0.2$ and high viscosity ratio to $m = 5$; $h^*_{w,2}$ for streamline plots (*a*), (*b*) and (*c*) is 0.40, 0.32 and 0.27, respectively; $h^*_{w,2}$ for (*d*), (*e*) and (*f*) is 0.40, 0.25 and 0.18, respectively.

along the mid lip surface. When the top layer is more viscous than the bottom layer, a recirculation of the bottom layer first appears, which grows until it touches the inter-layer. The separation point 'jumps' from the downstream to the upstream die corner, and mixing zone is formed.

Solutions at different density ratios, $r = \rho_1/\rho_2 = 2$ or 0.5 and non-zero interfacial tension $\sigma_I = 1\,\mathrm{dyne\,cm^{-1}}$ were also obtained, but there is no significant change in the inter-layer separation location and in the evolution of the flow states.

In sum, the predictions obtained with the finite element method explain the observed oscillation of the flow near the critical conditions for the onset of mid-gap invasion. The predicted critical bottom-layer thickness agrees well with the experiments; it is in the same range of the observations, e.g. $0.2 \lesssim h^*_{w,2} = h_{w,2}/H_g \lesssim 0.35$, and it falls weakly as the viscosity ratio rises. Moreover, the predictions reveal that the evolution of the flow states depends strongly on the viscosity ratio of the two liquid phases.

4. Mid-gap invasion: a simple model and the 1/3 rule

The evolution of the flow states as mid-gap invasion occurs at low and high viscosity ratios are shown in figure 13. Even though mid gap length is not much larger than the gap, e.g. $L_m/H_g = 2$, the streamlines strongly suggest that the flow under the mid lip can be effectively represented as a rectilinear flow for both invasion mechanisms. It is also important to notice that in both cases, mid-gap invasion is accompanied by flow reversal. In the low-viscosity-ratio regime, the flow reversal occurs in liquid phase 1 (top layer); in the high-viscosity-ratio regime, it occurs first in liquid phase 2 (bottom layer).

4.1. *Simple flow representation near the mid lip*

Since the flow is almost rectilinear, the velocity profile is approximately a superposition of Couette (drag by the moving substrate) and Poiseuille (pressure gradient along the bead) flows – quadratic velocity profile.

Figure 14 shows sketches of parabolic velocity profiles in the mid gap region at conditions before and after mid-gap invasion. Before mid-gap invasion, flow state (*a*) of figure 14, the mid gap region is filled with bottom-layer (layer 2) coating liquid. The adverse pressure gradient is not strong enough to cause flow reversal. As the bottom-layer flow rate falls, the adverse pressure gradient becomes stronger, and flow reversal occurs, as shown in figure 14(*c*), low-viscosity-ratio regime, and figure 14(*d*), high-viscosity-ratio regime.

The evolution of the velocity profile from (*a*) to (*c*) or (*d*) in figure 14, as bottom-layer (layer 2) flow rate decreases, must pass through flow state (*b*) which shows an inflection point of the velocity profile at the die lip. This event is the *onset of flow reversal*, and it can be related to the mid-gap invasion.

4.2. *The 1/3 rule, a simple criterion for onset of mid-gap invasion*

In order to derive a simple criterion to determine the critical conditions at the onset of mid-gap invasion, we will derive a simple criterion for the onset of flow reversal under the mid lip.

In rectilinear flow, the bottom-layer (layer 2) velocity profile is a combination of Couette and Poiseuille contributions, and it is a function of the pressure gradient across the mid lip $\Delta P/L_m$ and the web speed U_w:

$$u(y) = \frac{1}{2\mu_2}\left(\frac{\Delta P}{L_m}\right)(y^2 - H_g\, y) + \left(1 - \frac{y}{H_g}\right) U_w, \tag{4.1}$$

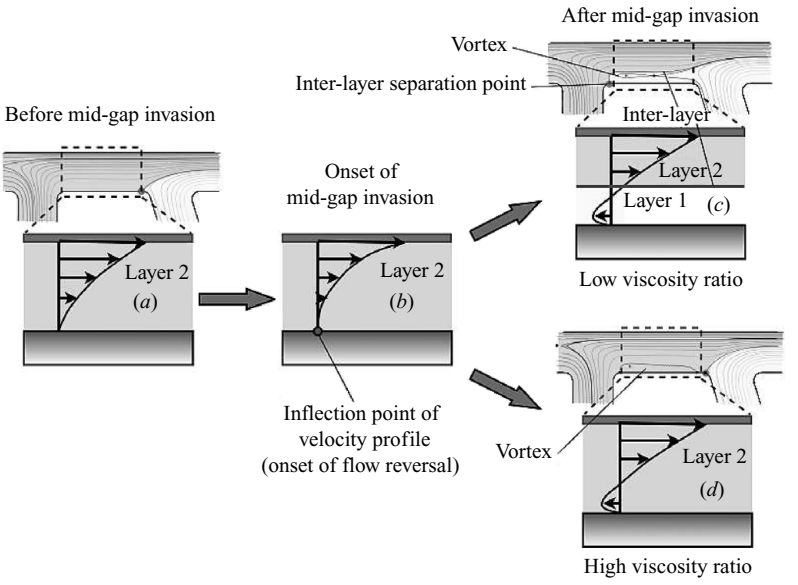

FIGURE 14. Evolution of the rectilinear velocity profile in the mid-gap region as mid-gap invasion occurs. The velocity profiles at the mid-gap invasion at low and high viscosities are shown in (*c*) and (*d*), respectively. The transition occurs when an inflection point in the velocity profile is located at the die surface (*b*).

where the subscript 2 stands for bottom-layer liquid; H_g is gap height; and y is the coordinate value defined from the moving substrate ($y = 0$) to the die lip ($y = H_g$).

At the onset of flow reversal, the velocity at the die lip has an inflection point, $(\mathrm{d}\,u(y)/\mathrm{d}\,y)|_{y=H_g} = 0$. One can extract the critical pressure gradient value at which this occurs:

$$\left(\frac{\Delta P}{L_m}\right)_c = \frac{2\,\mu_2\,U_w}{H_g^2}, \tag{4.2}$$

where the subscript c means the value is related to the onset of flow reversal.

The bottom-layer wet thickness can be related to pressure gradient through the bottom-layer flow rate, because the flow rate is the product of wet thickness and substrate speed in slot-coating method:

$$q_2 = \int_0^{H_g} u(y)\,\mathrm{d}y = -\frac{1}{12\mu_2}\left(\frac{\Delta P}{L_m}\right) H_g^3 + \frac{U_w}{2} H_g = h_{w,2}\,U_w, \tag{4.3}$$

where q_2 is the bottom-layer flow rate and $h_{w,2}$ is the bottom-layer wet thickness, as shown in figure 1.

At the onset of flow reversal, the critical dimensionless bottom-layer wet thickness, or flow rate, can be obtained by combining (4.2) and (4.3):

$$\left(h^*_{w,2}\right)_c = \left(\frac{h_{w,2}}{H_g}\right)_c = -\frac{H_g^2}{12\mu_2\,U_w}\left(\frac{\Delta P}{L_m}\right)_c + \frac{1}{2} = \frac{1}{3}. \tag{4.4}$$

This very simple argument shows that flow reversal occurs at $h^*_{w,2} = 1/3$; i.e. wet thickness of the bottom layer is 1/3 of the gap. As we have discussed before, flow reversal under the mid lip and mid-gap invasions are related phenomenon. The results from flow visualization and Navier–Stokes theory support this.

Even though the simple criterion cannot predict oscillations of inter-layer and the detailed mechanisms of mid-gap invasion and is based on strong simplifying assumptions; it provides a simple approximate coating window to avoid mid-gap invasion.

5. Conclusions

The stability of the separation point of the inter-layer in two-layer slot coating is directly associated with the quality of the final product. The location of the inter-layer separation point along the mid die lip as the operating conditions change was examined by both flow visualization and Navier–Stokes theory. From flow visualization, we found that the location of the separation point is a strong function of the bottom-layer flow rate and almost insensitive to the other operating parameters. The mid-gap invasion, the movement of the separation point from the downstream corner to the upstream corner of the mid lip, appears near the critical dimensionless bottom-layer flow rate around 0.3. It is always accompanied by an oscillation of the separation point.

Using Navier–Stokes theory, we constructed the G/FEM numerical model with two different mesh topologies to track the variation of the inter-layer position as the bottom-layer flow rate changed at different viscosity ratio. From the model, we discovered two different mechanisms – the onset of turn-around flow and the onset of microvortex – that depend on the viscosity ratio. They share an apparent similar visual phenomenon, the oscillation of the inter-layer due to high sensitivity of the flow state to the flow rate.

Furthermore, a simple flow model in the mid gap region is proposed based on lubrication theory. The model suggests that the appearance of an inflection point attached to the mid lip on the velocity profile signals the onset of mid-gap invasion. By combining the critical pressure gradient at the onset of flow reversal and the relationship between the bottom-layer flow rate and wet thickness, a simple criterion is derived: the onset of mid-gap invasion will occur when the dimensionless bottom-layer wet thickness is 1/3. This simple criterion is supported by the experimental evidences and the G/FEM model results.

We dedicate this work to Professor L. E. 'Skip' Scriven. He participated actively in the first steps of this research and unfortunately could not see its completion.

REFERENCES

Armi, L. 1986 The hydraulics of two flowing layers with different densities. *J. Fluid Mech.* **163**, 27–58.

Bolstad, J. H. & Keller, H. B. 1986 A multigrid continuation method for elliptic problems with folds. *SIAM J. Sci. Stat. Comput.* **7**, 1081–1104.

Cohen, D. 1993 Two-layer slot coating flow visualization and modelling. Master's thesis, University of Minnesota.

Maenosono, S., Okubo, T. & Yamaguchi, Y. 2003 Overview of nanoparticle array formation by wet coating. *J. Nanopart. Res.* **5**, 5–15.

Mavridis, H., Hrymak, A. N. & Vlachopoulos, J. 1987 Finite-element simulation of stratified multiphase flows. *AIChE J.* **33**, 410–422.

Musson, L. C. 2001 *Two-Layer Slot Coating* (PhD thesis, University of Minnesota). University Microfilms International.

Romero, J. R., Scriven, L. E. & Carvalho, M. S. 2006 Effect of curvature of coating die edges on the pinning of contact line. *AIChE J.* **52**, 447–455.

DE SANTOS, J. M. 1991 *Two-Phase Cocurrent Downflow Through Constricted Passage* (PhD thesis, University of Minnesota). University Microfilms International.

SARTOR, L. 1990 *Slot Coating: Fluid Mechanics and Die Design* (PhD thesis, University of Minnesota). University Microfilms International.

SARTOR, L., HUFF, S., KISHI, C. N., MEYER, D. & ERCILLO, J. C. 1999 Method of multilayer die coating using viscosity adjustment techniques. U.S. Patent 5 962075.

SCANLAN, D. J. 1990 Two-slot coater analysis: inner layer separation issues in two-layer coating. Master's thesis, University of Minnesota.

SCHLICHTING, H. & GERSTEN, K. 2001 *Boundary Layer Theory*, 8th edn. McGraw-Hill.

SILLIMAN, W. J. & SCRIVEN, L. E. 1980 Separating flow near a static contact line: slip at a wall and shape of a free surface. *J. Comput. Phys.* **34**, 287–313.

TAYLOR, S. D. & HRYMAK, A. N. 1999 Visualization and flow simulation of a two-slot coater. *Chem. Engng Sci.* **54**, 909–918.

THOMPSON, J. F., WARSI, Z. U. A. & MASTIN, C. W. 1985 *Numerical Grid Generation: Foundations and Applications*. North Holland.

VINOKUR, M. 1983 On one-dimensional stretching functions for finite-difference calculations. *J. Comput. Phys.* **50**, 215–234.

WILSON, MARK C. T., SUMMERS, JONATHAN L., KAPUR, N. & GASKELL, P. H. 2006 Stirring and transport enhancement in a continuously modulated free-surface flow. *J. Fluid Mech.* **565**, 319–351.